

Assessing solar energy potential using diurnal remote-sensing observations from Kalpana-1 VHRR and validation over the Indian landmass

Bimal K. Bhattacharya , N. Padmanabhan , Sazid Mahammed , R. Ramakrishnan & J.S. Parihar

To cite this article: Bimal K. Bhattacharya , N. Padmanabhan , Sazid Mahammed , R. Ramakrishnan & J.S. Parihar (2013) Assessing solar energy potential using diurnal remote-sensing observations from Kalpana-1 VHRR and validation over the Indian landmass, International Journal of Remote Sensing, 34:20, 7069-7090, DOI: [10.1080/01431161.2013.811311](https://doi.org/10.1080/01431161.2013.811311)

To link to this article: <https://doi.org/10.1080/01431161.2013.811311>



Published online: 15 Jul 2013.



Submit your article to this journal [↗](#)



Article views: 349



View related articles [↗](#)



Citing articles: 3 View citing articles [↗](#)

Assessing solar energy potential using diurnal remote-sensing observations from Kalpana-1 VHRR and validation over the Indian landmass

Bimal K. Bhattacharya^{a*}, N. Padmanabhan^b, Sazid Mahammed^b, R. Ramakrishnan^b,
and J.S. Parihar^a

^aEarth Ocean Atmosphere Planetary Sciences and Applications Area, Space Applications Centre (ISRO), Ahmedabad 380015, Gujarat, India; ^bSignal and Image Processing Area, Space Applications Centre (ISRO), Ahmedabad 380015, Gujarat, India

(Received 8 April 2012; accepted 11 March 2013)

A spectrally integrated clear-sky and three-layer cloudy-sky models were developed to determine atmospheric transmittances and instantaneous surface insolation. Half-hourly observations at 8 km spatial resolution in optical and thermal infrared bands from an Indian geostationary satellite (Kalpana-1) Very High Resolution Radiometer (VHRR) sensor were used to provide inputs to these models in addition to global 8 day aerosol optical depth and columnar ozone. Sensitivity analysis of the clear-sky model showed a higher influence of aerosol on global insolation, diffuse insolation, and its fraction as compared with water vapour and ozone. The root mean square error (RMSE) of insolation estimates of the daily integral was found to be 2.05 MJ m^{-2} ($\sim 11.2\%$ of measured mean) with a high correlation coefficient ($r = 0.93$) when compared with *in situ* measurements during 1 August 2008 to 31 March 2010 over six locations in India. The errors were found to reduce to 7.5% over 3 to 5 day averages. The comparison of annual estimates and equivalent reanalysis fields showed a mean difference of the order of $\pm 1.7 \text{ MJ m}^{-2}$ over the majority of the Indian landmass.

1. Introduction

Surface insolation is the driving input for two important eco-physiological processes: evapo-transpiration (Jacobs et al. 2000) and photosynthesis (Chen et al. 1999). In a climate system, insolation is the major contributor of radiation and energy budget of Earth and atmosphere. This drives the atmospheric circulation pattern. Generally, reflected parts of insolation from atmosphere, cloud, and Earth's surface contribute 6%, 20%, and 4% of insolation while there is 19% and 51% absorption of insolation by atmosphere–clouds and the Earth's surface, respectively. Insolation is also one of the most important renewable energy resources. In climate change adaptation and mitigation strategies, the use of solar energy plays an important role in maintaining an emission-free green and safe environment. Monthly solar radiation maps on a spatial scale are very important for locating solar energy conversion systems such as solar PV or thermal power plants (Janjai et al. 2005) and monitoring their performances on a real-time basis (Perez et al. 2001). The Jawaharlal Nehru National Solar Mission (JNNSM) is a major initiative by the Government of India

*Corresponding author. Email: bkbhattacharya@sac.isro.gov.in

to promote ecologically sustainable growth to address energy security challenges under India's national action plan on climate change. Conventionally, insolation maps are constructed from a high-density network of pyranometers. However, in a developing country, the network of pyranometer stations is sparse. Interpolation from such a network produces large errors (60–70%) due to large uncertainties of intermittent diurnal cloud cover, cloud types, and atmospheric turbidity in cloudless skies. Moreover, high maintenance costs and lack of availability of real-time data are major impediments. Generally, surface weather observatories for measuring routine weather elements are more than radiation-measuring stations. Therefore, during the 1970s and 1980s, surface insolation estimation models were largely dependent on temperature amplitude, sunshine hours, and a combination of temperature, humidity and rainfall, but these require site- and season-specific calibration of coefficients and thus are difficult to extrapolate over a larger region such as a country or continent. Moreover, such models do not explicitly consider the role of atmospheric constituents such as air molecules, aerosols, water vapour, and ozone. During the 1990s, a new set of attempts was made to estimate solar radiation in the ultraviolet region based on ozone content, elevation differences, and impact on the ecosystem (Alexandris et al. 1999; Katsambas et al. 1997; Kondratyev and Varotsos 1996; Varotsos 2005; Varotsos et al. 1995; Varotsos, Kondratyev, and Katsikis, 1995).

The use of remote-sensing observations from geostationary satellite sensors of high temporal sampling frequency (multiple passes every day) is ideal to capture the diurnal variability of atmospheric constituents such as water vapour, ozone, aerosols, and clouds, and thereby surface insolation on a continental scale. These are useful in those regions where regular measurements from a sparse radiation network and their availability have not been consistent. The preliminary comparison of satellite-based ozone estimates and Umkehr observations of the vertical ozone profile in the stratosphere showed promising results (Deluisi and Nimira 1978). Earlier analysis of cloud data from NASA's upper atmosphere research satellite over Polar regions led to the conclusion that the Arctic ozone hole will be equivalent to that of the Antarctic region by 2010 if stratospheric temperatures drop by 2–3°C. The area with low ozone over the North Pole was observed by several satellite sensors, e.g. the Ozone Monitoring Instrument on NASA's EOS-Aura and SCIAMACHY on the ENVISAT satellite. During 1 to 23 March in 2010 and 2011, the maps of ozone concentration in the Arctic showed a relatively higher ozone content in 2010 than in 2011 and the Arctic 'ozone hole' reached Scandinavia at the end of March, 2011 (Varotsos, Cracknell, and Tzani 2012). The Arctic has seen a marked reduction in sea-ice extent throughout the year, with a peak during the autumn. A new record minimum extent occurred in 2007, which was 40% below the long-term climatological mean (Turner and Overland 2009). There has been large-scale warming across much of the Arctic, with a resultant loss of permafrost and a reduction in snow cover. Therefore, there is a potential for release of methane from the Arctic region, especially through the thawing of permafrost and methane clathrates. Recent research carried out in 2008 in the Siberian Arctic has shown millions of tonnes of methane being released with concentrations in some regions reaching up to 100 times above normal. The oxidation of CH₄ produces HO_x radicals (here, HO_x = H + OH + HO₂), which catalyse ozone destruction cycles, particularly in the upper stratosphere (Revell et al. 2012). Moreover, a large amount of water vapour from the loss of sea-ice can be evaporated and injected in the stratosphere, which could cause large ozone losses in Polar regions through a chain of heterogeneous reactions involving inorganic chlorine (Anderson et al. 2012).

Broadly, two approaches, (1) statistical or empirical (Tarpley 1979; Noia, Ratto, and Festa 1993; Dedieu, Deschamps, and Kerr 1987; Illera, Fernandez, and Perez 1995; Laurens et al. 1995) and (2) physical or radiative transfer (Tanahashi et al. 2001; Lu et al. 2010) schemes, are in use to estimate surface insolation using geostationary satellite data. Empirical or statistical techniques for surface insolation include Heliosat (Dagestad 2004) and contrast ratio (Rosema et al. 2004) approaches applied to Meteosat. Physical modelling schemes of clear-sky insolation are of two types: (1) a 'top-down' approach that corrects incoming solar irradiance (Pinker and Laszlo 1992; Pinker, Frouin, and Li 1995) for atmospheric attenuation (absorption and scattering) before reaching the surface; and (2) a 'bottom-up' approach that determines surface albedo (Gautier, Diak, and Masse 1980) from planetary albedo by separating out atmospheric interference and arrives at surface insolation through inversion. Several schemes are available to account for the attenuation of solar radiation flux passing through clouds. While the errors of statistical techniques varied from 12% to 17% for daily total insolation (Kandirmaz et al. 2004), the physical approach produces an error of about $\pm 19\%$ on an hourly basis and a smaller one for daily to monthly averaging.

The Kalpana-1 (K1) is an exclusive meteorological satellite in the Indian National Satellite (INSAT) system, which was launched on an augmented Polar Satellite Launching Vehicle (PSLV) to locate in geostationary orbit. The satellite consists of a very high resolution radiometer (VHRR) payload with a data relay transponder (DRT) to provide meteorological services. This radiometer consists of one broad VIS (visible, 0.55–0.75 μm), one water vapour (WV, 5.7–7.1 μm), and one thermal infrared (IR, 10.5–12.5 μm) band. The INSAT Meteorological Data Processing System (IMDPS) (Anonymous 2005) provides both 'full-globe' and 'sector' data products in all three bands at half-hour intervals at 8 km spatial resolution in an automated mode. So, there is a maximum of 48 acquisitions on a given day.

To date, no digital maps of daily and monthly surface insolation have been available over India and some of its adjacent parts using observations from Indian geostationary satellites with region-specific model parameters. This was also considered to be deficient while assessing solar energy potential in India by the Ministry of Renewable Energy Resources (MNRE), Government of India. Moreover, regular updates are needed to know and correlate intra- and inter-seasonal differences in the radiation-energy budget with water use, agricultural productivity, and the bio-geochemical cycle. This can be achieved on a real-time basis if surface insolation is generated through an automated operational chain. These are the basic drivers of motivation of the present article. However, the algorithm calls for testing and evaluation before product generation through the operational chain.

The present article highlights the features of a spectral irradiance model for clear-sky (cloudless) and a three-layer cloudy-sky model for the estimation of instantaneous, daily, and monthly surface insolation over southeast Asia using cloud and water vapour inputs from Kalpana-1 VHRR and ancillary inputs from global aerosol, ozone, and elevation. The study was carried out with the following objectives.

- (1) To define a new robust physical algorithm for surface insolation estimation using observations from Indian geostationary satellite (Kalpana-1) sensor (VHRR) and to test the sensitivity of the clear-sky model.
- (2) To validate surface insolation estimates against *in situ* measurements and compare with a monthly reanalysis product.

2. Study area and data set

2.1. Indian geostationary satellite data

Half-hourly data of Kalpana-1 VHRR (K1VHRR) Asia Mercator sector (44.5° E–105.3° E, 9.8° S–45.5° N) were acquired through the Meteorology and Ocean Satellite Data Archival Centre (MOSDAC) for the period 1 August 2008 to 31 March 2010 (<http://www.mosdac.gov.in>). Raw data after reception at each acquisition were corrected for servo, line-loss, radiometry, stagger, and oversampling removal using the INSAT/Kalpana-1 data products scheduler. This results in automated generation of co-registered data in each band at Transverse Mercator (TM) projection. The dimension of each band at each acquisition is 808 rows \times 807 columns for the Asia Mercator sector product. The data were in hierarchical data format 5 (h5). Each h5 data set contains digital co-registered binary data in VIS, WV, and thermal infrared (TIR) bands at 8 km spatial resolution at TM projection, angular geometry (sun's zenith, azimuth, view zenith, azimuth, and relative azimuth), look-up table (LUT) for conversion of WV and TIR data to radiances and brightness temperatures and pixel-wise latitude and longitude. A maximum of 48 slots in a day were acquired.

2.2. Ancillary global data

The ancillary data consist of 8 day global atmospheric products (1° \times 1°) averaged from MODIS TERRA and AQUA on total columnar ozone and aerosol optical depth at 550 nm (AOD₅₅₀). Different versions of AOD₅₅₀ such as the mean of land–ocean aerosols, ocean-blue aerosols, and corrected land aerosols were used to fill up gaps in areas of desert and some ocean regions. Since no aerosol data are available from INSAT/Kalpana-1 VHRR, only available global products on ozone and AOD₅₅₀ were resampled to 8 km through bilinear interpolation for Asia Mercator region and then reprojected at TM projection before their use. Global elevation database from GTOPO5 at 1 km were resampled to 8 km for the Asia Mercator region and reprojected to TM projection before use.

2.3. In situ measurements

Half-hourly average incoming shortwave radiation was measured through a four-component net radiometer (model CNR 1) placed at 2 m height on five prototype 10 m micrometeorological towers (popularly known as the Agro-Met Station (AMS)) powered through solar panels. These towers had an INSAT communications link (Bhattacharya, Dutt, and Parihar 2009) for uplinking and downlinking continuous data streams measured over any remote location within the footprint coverage of the DRT. These prototype towers were located (Table 1) at Nawagam and Junagadh in the Gujarat province of western India, Bijapur in Karnataka province in southern India, the Forest Research Institute (FRI), Dehradun, in the Uttarakhand province of northern India, and Hyderabad in Andhra Pradesh province of India. The data were obtained from August 2008 to May 2009 at the first three stations, and a few data sets during January to March 2010 at FRI, Dehradun. Consistent half-hourly data were further used to produce a daily integral using trapezoidal integration (Gautier, Diak, and Masse 1980).

At Birla Institute of Technology (BIT), Ranchi (Jharkhand province), eastern India, incident shortwave radiation was measured at 1 minute intervals through a four-component net radiometer (model CNR 1) placed at 2 m height in an eddy tower. Data were averaged over a day, and daily averaged data were obtained for January 2008 to March 2010. The daily averages were converted to daily integral in MJ m⁻². The stations represent a wide

Table 1. Summary of geographic locations of *in situ* measurement stations.

Station	(°N)	(°E)	Elevation (m)	Validation reference
Bijapur, Karnataka (semi-arid)	16.82	75.75	575	ISRO-AMS
FRI, Dehradun, Uttarakhand (humid)	30.33	78.00	3503	ISRO-AMS
Junagadh, Gujarat (sub-humid)	21.50	70.44	85	ISRO-AMS
Nawagam, Gujarat (semi-arid)	22.8	72.57	29	ISRO-AMS
BIT, Ranchi, Jharkhand (humid)	23.42	85.44	614	Eddy tower
Hyderabad, Andhra Pradesh (semi-arid)	17.36	78.37	540	ISRO-AMS

Note: Text in parentheses denotes type of climate at measurement location.

range of climate, from semi-arid to humid and are distributed over plain, plateau, and valley lands with elevation varying from 29 to 3503 m. The data period covers the four seasons of spring–summer, summer–monsoon, autumn, and winter.

3. Methodology

The algorithm uses a clear-sky model with a spectrally integrated radiative transfer scheme that requires solar zenith angle, elevation, slope, aspect of terrain, aerosol, water vapour, and ozone as inputs. This accounts for the depletion of instantaneous incoming solar radiation flux due to atmospheric perturbation or turbidity. In cloudy sky, a separate three-layer scheme was implemented where cloud is assumed to be plane parallel sandwiched between upper and lower cloudless atmospheric layers.

3.1. Clear-sky model

3.1.1. Direct or beam irradiance

A simple but accurate spectral irradiance model (Paulescu and Schlett 2003) was used to determine instantaneous direct or beam irradiance (in W m^{-2}) over the entire shortwave range (0.3–3.0 μm). An integrated spectral (10 nm interval) atmospheric transmittance scheme developed by them was used in the present study. The instantaneous direct or beam irradiance (S_{dir}) over the entire shortwave region was computed in W m^{-2} as

$$S_{\text{dir}} = S_0 \tau_{\text{R}} \tau_{\text{oz}} \tau_{\text{w}} \tau_{\text{g}} \tau_{\text{A}}, \quad (1)$$

$$S_0 = E_0(1 + 0.0344 \cos(360(N/365))), \quad (2)$$

where τ_{oz} = ozone transmittance, τ_{R} = Rayleigh transmittance, τ_{w} = water vapour transmittance, τ_{A} = aerosol transmittance, τ_{g} = transmittance of other gases, E_0 = solar constant (1367 W m^{-2}), S_0 = instantaneous irradiance (W m^{-2}) at top-of-atmosphere, and N = calendar day.

The Rayleigh transmittance, τ_{R} , was computed as

$$\tau_{\text{R}} = \exp[-0.008735\lambda^{-4.08}m_p]. \quad (3)$$

The τ_{R} was computed over a 10 nm interval and integrated over the whole shortwave spectrum. The digital elevation model was used to compute m_p and the Rayleigh transmittance

for each pixel. Here, m_p is the optical air mass at a given atmospheric pressure ‘ p ’ and λ is the wavelength (μm).

The relative optical air mass, m , is computed as

$$m = 1/[\cos\theta_s + 0.15(93.885 - \theta_s)^{-1.253}], \quad (4)$$

where θ_s = solar zenith angle.

The generalized form of integrated spectral transmittance for a given atmospheric quantity, x , has the following functional form:

$$\tau(x) = \exp[-x(a + bx + cx^d)]. \quad (5)$$

Here, $x = ml$ for ozone (l = ozone content in atm-cm); $x = mw$ for water vapour (w = atmospheric precipitable water or columnar water vapour in g cm^{-2}); $x = m$ for other atmospheric gases (g); and $x = m\beta$ for aerosol (β = Angstrom’s turbidity factor characterizing atmospheric visibility of haziness based on given aerosol type and size distribution). a , b , c , and d are parameters for every extinction process. The values are taken from Paulescu and Schlett (2003) as given in Table 2.

3.1.2. Diffuse irradiance

The instantaneous diffuse irradiance (s_{diff}) is contributed from three components, (1) molecular (Rayleigh) scattering (s_{R}), (2) aerosol scattering (s_{A}), and (3) multiple scattering (s_{M}) of ground reflected radiation from atmosphere:

$$s_{\text{diff}} = s_{\text{R}} + s_{\text{A}} + s_{\text{M}}, \quad (6)$$

$$s_{\text{M}} = (s_{\text{dir}} + s_{\text{R}} + s_{\text{A}})((\rho_{\text{g}} \rho_{\text{a}})/(1 - \rho_{\text{g}} \rho_{\text{a}})), \quad (7)$$

$$s_{\text{R}} = 0.79s_0\tau_{\text{oz}}\tau_{\text{g}}\tau_{\text{w}}(1 - (1 - w_0)(1 - m + m^{1.06})(1 - \tau_{\text{A}}))0.5(1 - \tau_{\text{R}})/(1 - m + m^{1.06}), \quad (8)$$

$$s_{\text{A}} = 0.79s_0\tau_{\text{oz}}\tau_{\text{g}}\tau_{\text{w}}(\tau_{\text{A}}/(1 - (1 - w_0)(1 - m + m^{1.06})(1 - \tau_{\text{A}}))) \times f_c(1 - (\tau_{\text{A}}/(1 - (1 - w_0)(1 - m + m^{1.06})(1 - \tau_{\text{A}}))))\tau_{\text{R}}/(1 - m + m^{1.06}), \quad (9)$$

where w_0 = single scattering albedo assumed as 1.0.

Table 2. Summary of parameters for different atmospheric components influencing radiative transfer through the atmosphere (Paulescu and Schlett 2003).

Atmospheric variable	a	b	c	d
Ozone (l)	0.0184	0.0004	0.022	-0.66
Water vapour (w)	0.002	1.67×10^{-5}	0.094	-0.693
Other gases (g)	-5.4×10^{-5}	-3.8×10^{-6}	0.0099	-0.62
Aerosol (β)	1.053	-0.083	0.3345	-0.668

The atmospheric albedo, ρ_a , was determined as

$$\rho_a = 0.0685 + (1 - f_c) (1 - (\tau_A / (1 - (1 - w_0) (1 - m + m^{1.06}))(1 - \tau_A))) \tau_R. \quad (10)$$

The ratio (f_c) of forward to backward scattering was determined as

$$f_c = 0.9302 \cos(\theta_s)^2. \quad (11)$$

Columnar water vapour (w) required to compute water vapour transmittances was estimated from a semi-empirical equation developed by Bhattacharya et al. (2010) based on differences in brightness temperatures in thermal IR and WV channels of Kalpana-1 VHRR. The aerosol optical depth at 550 nm from the MODIS product was converted to the Angstrom ‘ β ’ turbidity parameter to compute aerosol transmittance assuming the Angstrom turbidity exponent parameter to be 1.3 (Iqbal 1983). The ozone data from MODIS were used to compute ozone transmittance.

The monthly minimum ground brightness from the previous 30 day VIS band planetary albedo (ρ_{VIS}) was dynamically determined for each acquisition and was used as a surrogate for ground albedo (ρ_g). The planetary VIS band spectral albedo was corrected for Rayleigh scattering. The aerosol scattering effect and cloud interference on planetary albedo were assumed to be removed with monthly minimum composites providing that surface properties did not change significantly within 30 days. The multiple scattering component contributes little to total diffuse irradiance over a vegetated region (albedo between 0.1 and 0.3) but is a dominant component over snowbound areas or desert (>0.3) with significantly higher albedo.

3.1.3. Global or total irradiance

Both direct and diffuse irradiance are dependent on the zenith angle of the Sun, which changes from sunrise to sunset, and on the orientation of the surface. On an arbitrarily inclined surface, with slope α and aspect φ , at a given location on Earth’s surface with latitude ϕ , the angle (i) between the incident radiation and the normal to the surface is expressed as

$$\cos i = \sin \delta (\sin \cos - \cos \sin \alpha \cos \varphi) + \cos \delta \cos h (\cos \cos \alpha + \sin \sin \alpha \cos \varphi) + \cos \delta \sin \alpha \sin \varphi \sin h, \quad (12)$$

$$\delta = 23.45 \sin(360(284 + N)/365), \quad (13)$$

where δ = solar declination angle (radian) and h = sun hour angle (radian).

Depending on both terrain properties and solar geometry, the surface may be in the shadow of nearby topographic features; $\cos i$ is then assigned a value of zero that represents no direct irradiances. Diffuse radiation was assumed to be isotropic in distribution in the atmosphere, i.e. the sky is uniformly bright. Depending on the slope and nearby topography, only a fraction of the hemisphere might be visible, which is referred to as the sky-view factor (V_d), which is time invariant and is dependent only on terrain parameters. The total (S_{tot}) or global irradiance ($W m^{-2}$) received on the surface at any instance (t) is given by

$$S_{tot(t)} = S_{dir(t)} \cos i(t) + S_{diff(t)} V_d. \quad (14)$$

V_d is determined as the ratio of diffuse sky irradiance to that on an unobstructed surface. In the present algorithm, this was computed using the expression given by Kondratyev (1977):

$$V_d = (1 + \cos\alpha)/2. \quad (15)$$

3.2. Cloudy-sky model

A three-layer scheme was conceptualized and implemented to compute irradiances in cloudy skies. The first layer corresponds to a clear-sky atmosphere over the cloud-top, where direct and diffuse components were computed using the algorithm mentioned in Section 3.1. Molecular (above cloud) and aerosol scattering and gaseous transmission due to ozone were considered. All aerosols and ozone were assumed to be distributed above the cloud. Both direct and diffuse components were computed and the sum of these two resulted in global irradiances without any sky-view factor. The second layer corresponds to plane parallel cloud. The vertical cloud structure and its three-dimensional effects on cloud transmission, especially on the diffuse component, were not considered in the present model. The third layer corresponds to clear-sky atmosphere below cloud. Molecular scattering (air below cloud) was only considered in layer 3. Precipitable water was assumed entirely distributed below cloud and contributed to gaseous transmission along with other gases.

In order to compute Rayleigh scattering above cloud, the height of the cloud-top was approximated from cloud-top temperature, maximum clear-sky planetary temperature within the previous 30 days, ground elevation, and dry-adiabatic lapse rate up to condensation level represented through cloud-top temperature. Here also, direct, diffuse, and global irradiances were computed using the principles shown in Section 3.1. The irradiance coming from the first and top clear-sky layer after attenuation is considered as the incoming solar radiation flux to the cloud layer. The energy flux that comes out after being attenuated in the cloud layer is considered as the influx for the third layer (clear-sky layer below cloud), which again becomes attenuated to reach the ground. Global irradiance received at the ground is considered as insolation in a cloudy sky.

Transmission through cloud was computed using the Kubelka–Munk theory:

$$t_c = a \exp(-bA_c). \quad (16)$$

This relates cloud-top albedo (A_c) with cloud transmittance (t_c). The coefficients (a , b) in Equation (16) vary according to different land-use categories that were taken into account through typical ranges (<0.2 for waterbodies and forest; 0.21–0.32 for agriculture; >0.3 for desert and snow cover) of ground albedo represented by minimum ground brightness from the previous 30 days.

3.3. Daily integration

A trapezoidal integration was applied to construct the daily integral from diurnal instantaneous global irradiances. The daily integral global irradiance S_d was expressed in MJ m^{-2} . The mathematical expression for daily integration is

$$S_d = 0.864 \sum_{i=0.5}^{23.5} (S_{(i-0.5)} + S_{(i)})/2. \quad (17)$$

This insolation model is named KIRAN (Kalpana-1 incident solar radiation).

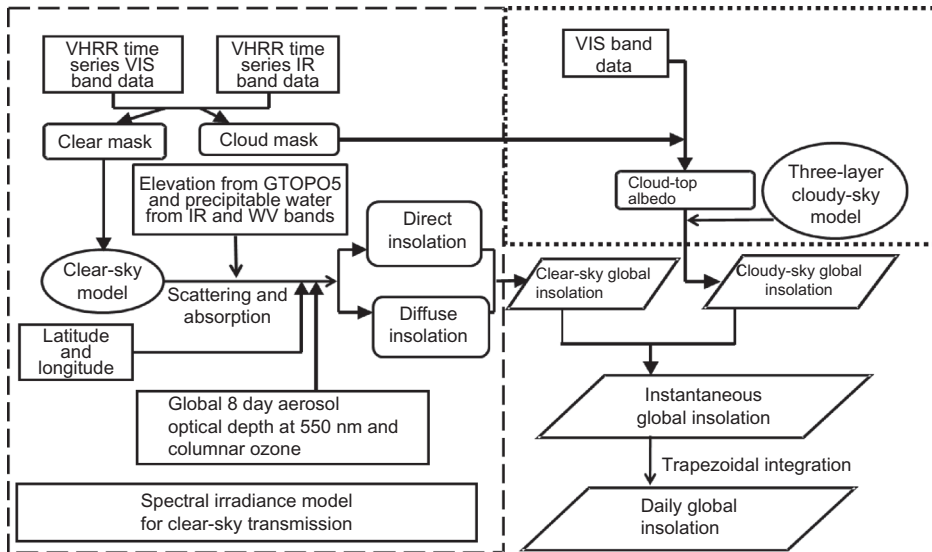


Figure 1. Pathway for estimating instantaneous and daily global surface insolation from K1VHRR observations and ancillary data using clear-sky and cloudy-sky models.

Here, i represents hours in GMT. The whole pathway of instantaneous insolation and daily integration is shown in Figure 1.

The features unique to KIRAN as compared with pre-existing models are as follows.

- (1) Atmospheric water vapour was estimated from an empirical formulation developed over the Indian region between the difference in brightness temperatures of WV and thermal IR bands and sounder-based precipitable water.
- (2) In the three-layer cloudy-sky model, the assignment of approximate cloud height for computing Rayleigh transmittance above cloud was done based on the minimum ground brightness temperature from the previous 30 days at a given acquisition time, dry adiabatic lapse rate, and cloud-top temperature in the current acquisition.
- (3) A shifting and continuously updated bi-spectral threshold determined from the previous 30 days for a given acquisition time was implemented for cloud detection rather than using fixed thresholds for a month. It requires the previous 30 day data to initiate the computation, but it generates output in a real-time mode. Additional criteria for detecting thin clouds and thin fogs were applied when the cloudiness index crossed 0.15. This index was internally generated for every acquisition from the ratio of difference in current VIS albedo and minimum ground brightness and difference in maximum VIS albedo and minimum ground brightness.

3.4. Scripting of KIRAN and implementation

The entire chain of computational steps was scripted in C-language with one main program and three sub-programs.

3.4.1. Inputs on geostationary, ancillary data and pre-processing

The first sub-program unpacks h5 data sets from K1VHRR, reads digital elevation data, and computes date, time and year from the name of the file string as well as interpolating

sun-sensor zenith and azimuth angles. Brightness temperatures in IR and WV bands and VIS band planetary albedo (after removing perturbation due to molecular scattering) were also computed from the LUT provided with h5 data sets.

3.4.2. Interpolation of gridded AOD, ozone, and resampling

Another sub-program uses 8 day gridded ($1^\circ \times 1^\circ$) AOD and ozone averaged from MODIS TERRA (1100 LMT) and AQUA (1330 LMT) to extract from global products for the latitude and longitude bounds of southeast Asia corresponding to K1VHRR Asia Mercator sector coverage. These were resampled to 8 km spatial resolution using bilinear interpolation. Later, these were resampled to TM projection. The resampled atmospheric products were generated for 2008, 2009, and up to the end of March of 2010 prior to final insolation processing.

3.4.3. Generation of maximum and minimum ground reflectivity and brightness temperatures, and cloud/fog mask generation

This sub-program uses K1VHRR brightness temperatures and VIS band planetary albedo or reflectivity from a lead period of the previous 30 days. The minimum Rayleigh corrected planetary albedo and maximum temperatures were picked up for each pixel at a given acquisition. The minimum reflectivity and maximum brightness temperatures with some 5% confidence margin serve as thresholds (Schadlich, Gottesche, and Olesen 2001) to detect the presence of clouds or fog. A pixel is flagged cloudy/foggy when current-day planetary albedo at a given acquisition exceeds its threshold albedo and brightness temperature is below the threshold. The lead period moves dynamically with advancement of each day while updating both thresholds pixel-by-pixel.

3.4.4. Generation of time series diurnal instantaneous insolation

The main program computes time series instantaneous global (direct and diffuse combined) insolation for a given acquisition using the outputs from other sub-programs, clear-sky models, and cloudy-sky models.

3.4.5. Integration

Daily integration of instantaneous insolation using trapezoidal integration (please refer to Section 3.3). This program fetches instantaneous insolation from different acquisitions on a given day and makes a list. The program first checks at least one acquisition within 3 hours and then daily integration is performed. It means that if at least five well-distributed instantaneous insolutions are available during daytime hours in the list, the integration is performed.

4. Results

4.1. Sensitivity of clear-sky model

The responses of the clear-sky model on global, direct, and diffuse instantaneous insolation, direct-diffuse ratio, diffuse fraction to variation in solar zenith angle, atmospheric ozone, water vapour, and AOD at 550 nm were studied. This was carried out with the observed

seasonal range of AOD, water vapour, and ozone over Bijapur station. The effects of change in aerosol optical depth at 550 nm (AOD_{550}) were studied at low ($10\text{--}20^\circ$) and high ($40\text{--}70^\circ$) levels of solar zenith angles (Figure 2). There was a substantial and similar trend of decrease in both global (15–20%) and direct (25–30%) instantaneous insolation for a given range of AOD_{550} (0.05 to 0.6), but the gap between direct and global is reduced at a higher solar zenith angle. The steepness of slopes of direct insolation was more negative (-0.67 W m^{-2}) than global insolation (-0.35 W m^{-2}). The slopes were less negative (-0.48 W m^{-2} , -0.35 W m^{-2}) at higher solar zenith angles for both cases. Diffuse insolation, in general, showed a gradual increase with increase in AOD_{550} but it reached a plateau at a

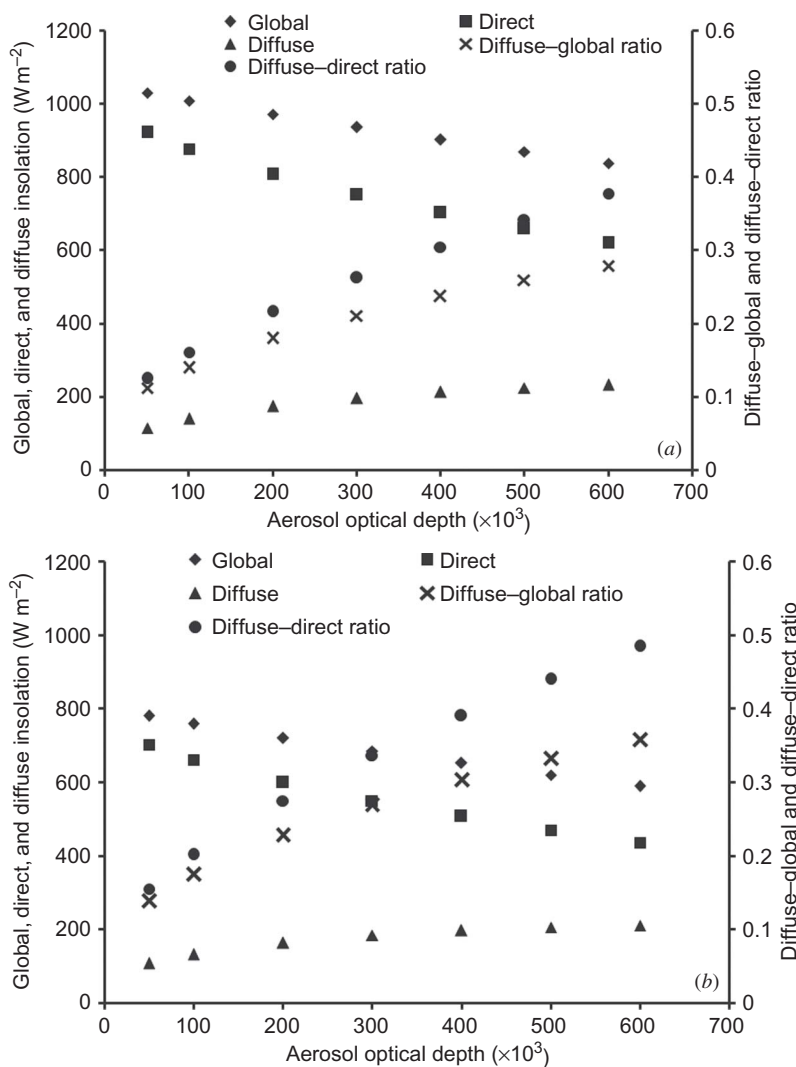


Figure 2. Sensitivity of aerosol on global insolation, its components and ratios for (a) solar zenith angle = 17.76° , precipitable water = 4.47 cm, ozone = 270 Dobson units; (b) solar zenith angle = 41.1° , precipitable water = 4.47 cm, ozone = 270 Dobson units at Bijapur station (16.82° N , 75.75° E , elevation of 603 m above mean sea level).

higher solar zenith angle with AOD₅₅₀ beyond 0.2. The diffuse fraction was found to show a sharp increase between 0.12–0.28 and 0.18–0.38 at low (17.46°) and high (41.1°) solar zenith angles with increase in AOD₅₅₀ from 0.1 to 0.6. But the higher diffuse fraction was noticed at higher solar zenith angles for similar AOD₅₅₀. It was found that there was practically little decrease (3–7%) in global, direct, and diffuse insolation with increase in water vapour from 1.5 to 6.5 cm (Figure not shown). The decrease was still less for ozone (Figure not shown) for the variation of ozone concentration from 240 to 290 Dobson units.

4.2. Validation

The K1VHRR daily insolation estimates averaged over 3×3 pixels centred over ISRO-AMS and eddy tower locations were compared with *in situ* measurements from a CM3 pyranometer. The selection criteria for choosing quality validation data sets are described below.

- (1) Days with daily insolation estimates constituted from at least one instantaneous insolation per three hours from 0000 GMT to 1300 GMT are only used for validation. These maintain diurnal symmetry to produce reliable daily integral.
- (2) The days with *in situ* continuous half-hourly measurements are retained for validation. The days with any data loss due to communication failure are rejected.

After applying these criteria, the rejected paired data sets were found to be 17.5% (25 out of 143) for Bijapur, 27% (17 out of 63) for Dehradun, 19% (31 out of 165) for Junagadh, 35% (72 out of 208) for Nawagam, 20% (22 out of 110) for Hyderabad, and 25% (50 out of 198) for Ranchi. The error analysis showed that the root mean square error (RMSE) varied from 1.41 to 2.41 MJ m⁻² (Table 3), while mean absolute error (MAE) and mean deviation (MD) or mean bias were found to vary from 1.15 to 2.08 MJ m⁻² and from -0.12 to 1.73 MJ m⁻², respectively. Both MAE and RMSE were the highest in Ranchi as compared with

Table 3. Error statistics of K1VHRR daily insolation estimates with respect to *in situ* measurements.

Station	Latitude (°N)	Longitude (°E)	Elevation (m)	Validation reference	<i>r</i>	Error statistics (MJ m ⁻²)		
						MD	MAE	RMSE
Bijapur	16.82	75.75	575	ISRO-AMS	0.94	1.73	1.96	2.24(11.3%)
Dehradun	30.33	78.00	3503	ISRO-AMS	0.94	0.66	1.15	1.41(8.3%)
Junagadh	21.50	70.44	85	ISRO-AMS	0.96	-0.12	1.26	1.53(9.0%)
Nawagam	22.8	72.57	29	ISRO-AMS	0.94	0.45	1.57	1.87(10.1%)
Ranchi	23.42	85.44	614	Eddy tower	0.89	1.00	2.08	2.41(12.9%)
Hyderabad	17.36	78.37	540	ISRO-AMS	0.93	1.00	2.01	2.27(11.4%)

Notes: MD, mean deviation; MAE, mean absolute error; RMSE, root mean square error. RMSE is expressed as a percentage (within parentheses) of measured mean; *r*, correlation coefficient.

$$MD = \left[\sum_i^n (P_i - O_i) \right] / n; MAE = \left[\sum_i^n \text{abs}(P_i - O_i) \right] / n; RMSE = \sqrt{\left[\sum_i^n (P_i - O_i)^2 \right] / n}$$

Here, P_i , i th predicted insolation from the satellite; O_i , i th observed or measured insolation from the pyranometer; abs refers to absolute value; ISRO-AMS, half-hourly data were available in W m⁻², which were converted to daily integral in MJ m⁻²; eddy tower, daily average insolation was obtained, which was converted to daily integral in MJ m⁻².

Table 4. Regional statistics of monthly mean insolation based on the year 2009.

Month	Regional statistics				
	Minimum (MJ m ⁻²)	Maximum (MJ m ⁻²)	Range (MJ m ⁻²)	Mean (MJ m ⁻²)	Standard deviation (MJ m ⁻²)
January	1.66	26.89	25.23	13.35	6.12
February	4.08	27.91	23.83	16.38	6.13
March	5.58	27.18	21.60	17.84	5.17
April	4.20	26.66	22.46	18.87	4.18
May	8.19	27.22	19.03	19.12	2.66
June	8.33	29.09	21.06	19.15	3.05
July	7.40	28.00	20.60	17.47	3.19
August	10.29	26.92	16.63	18.35	2.54
September	5.85	27.20	21.35	18.50	3.80
October	4.38	24.88	20.50	16.00	4.38
November	1.11	28.24	27.13	14.63	6.97
December	1.19	27.23	26.04	13.35	6.25

other stations. The mean bias was positive in four out of five stations but it is low and negative in Junagadh. The mean positive biases were lower in Nawagam (0.45 MJ m⁻²) and Dehradun (0.66 MJ m⁻²) as compared with biases in Bijapur (1.73 MJ m⁻²) and Ranchi (1.00 MJ m⁻²). The correlation coefficient was found to be higher (0.94–0.96) for ISRO-AMS stations as compared with the lone eddy station in Ranchi. The RMSE, MAE, and mean bias of pooled data sets were 2.05 MJ m⁻² (11.2% of measured mean), 1.71 MJ m⁻², and 0.74 MJ m⁻², respectively, with a correlation coefficient of 0.92 (Table 4). These are relatively less by 1.86 MJ m⁻² (10.4% of measured mean), 1.55 MJ m⁻², and 0.62 MJ m⁻², respectively for pooled data sets with all AMS stations (Table 4) only. The correlation was also higher (0.94). The errors from VHRR estimates were close to those reported by Otkin et al. (2005) over the USA (10%) using Geostationary Operational Environmental Satellite (GOES) observations and by Lu et al. (2010) over China (17.7%) using Geostationary Meteorological Satellite (GMS) data.

The validation data sets from Ranchi station were obtained as 24-hour daily averages in W m⁻² from 1 minute time sampling. These were converted to daily integral in MJ m⁻² through a conversion factor. For ISRO-AMS, data were obtained as half-hourly averages throughout the daylight hours and were later integrated to daily sum in the same way as for K1VHRR daily estimates from instantaneous insolation. The difference in methodology of producing daily integrals is the major reason for showing more RMSE and reduced correlation for BIT, Ranchi. The plot of pooled validation is shown in Figure 3.

Further analysis was carried out to investigate the averaging effect on validation results. It was found that the RMSE of insolation estimates at BIT, Ranchi, was found to be reduced from 11.2% to 7.5% as the averaging period increased from daily to 5 day, and correlation coefficient increased from 0.92 to 0.96.

4.3. Sources of uncertainties in the estimates

The possible sources of uncertainties that contribute to errors in K1VHRR daily insolation estimates are outlined in the following sub-sections.

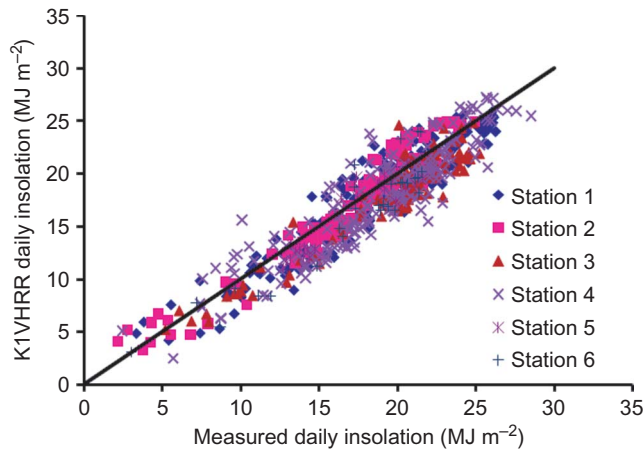


Figure 3. Validation of K1VHRR daily insolation estimates with *in situ* measurements. Here, Stations 1 to 6 represent pyranometer sites at Nawagam (Gujarat province), Junagadh (Gujarat province), Bijapur (Karnataka province), Ranchi (Jharkhand province), Dehradun (Uttarakhand province), and Hyderabad (Andhra Pradesh province) on the Indian sub-continent. The RMSE of daily insolation estimates is 2.05 MJ m^{-2} (11.2% of measured mean), correlation coefficient (r) = 0.92, number of data sets = 665.

4.3.1. Diurnal aerosol properties

Sensitivity analysis showed little influence of ozone and water vapour content on insolation at different solar zenith angles, but strong sensitivity of AOD at 550 nm was observed on insolation. Single scattering albedo was assumed to be 1.0 in the present model, but in reality it varied from 0.7603 to 0.9921 among urban–rural–ocean aerosol types (Li 1998). In the present model, an 8 day global AOD product from the average of MODIS TERRA and AQUA was used rather than diurnal AOD. Moreover, the $1^\circ \times 1^\circ$ gridded data were resampled down to the K1VHRR spatial scale. It lacks sub-grid heterogeneity in aerosol properties. These factors could lead to errors in insolation estimates.

4.3.2. Scale mismatch between estimates and measurements

The insolation product was generated at an 8 km spatial scale, which may not sometimes capture the sub-pixel variability of thin haze, clouds, early-morning or late-afternoon fog, and their influence on insolation that could have been captured through pyranometers at the tower footprint scale of a few metres. The use of estimates averaged over 3×3 pixels for validation with measurements at the tower footprint scale may be valid for cloudless skies, but it may lead to underestimation if cloud patches are present and irregularly distributed in the surrounding pixels but not in the central pixel. It may lead to overestimation if cloudy patches are only present in the central pixel representing the tower location but not in the surrounding pixels.

4.3.3. Difference in temporal sampling

The ISRO-AMS observations on incident shortwave radiation were sampled at five-minute intervals and averaged over 30 minutes. K1VHRR samples with instantaneous snapshots were at 30 minute intervals. Therefore, it misses out intermittent cloud presence and its

spatio-temporal dynamics. These differences must have introduced some uncertainties in the validation results.

4.3.4. *Inherent weakness in cloudy-sky model*

In the three-layer cloudy sky model, the middle layer is cloud assumed as plane parallel that separates upper and lower cloudless layers. The three-dimensional (3D) extent (Varnai and Marshak 2002) of clouds, their microphysical properties, and their separate radiative effects on direct and diffuse transmittances have not been considered.

4.3.5. *Lack of representation of chemical coupling among atmospheric GHGs*

In the present insolation model, greenhouse gases (GHGs) were treated as other gases without having partitioning of radiative forcing by individual GHGs, atmospheric particulate matter, and their likely impact through chemical coupling with ozone. Carbon dioxide (CO₂), the dominant anthropogenic GHG, elevates ozone by cooling the stratosphere, which slows the gas-phase ozone loss cycles. Of the GHGs controlled under the Kyoto Protocol, those with the highest radiative forcing after CO₂ are N₂O and CH₄, both of which lead to changes in ozone via chemical processes. Consequently, reactive nitrogen species produced from N₂O and reactive hydrogen species produced from CH₄ are expected to play an increasingly important role in determining stratospheric ozone concentrations. Although the roles of N₂O and CH₄ in ozone chemistry are qualitatively understood, the sensitivity of ozone to these gases has not been thoroughly investigated. N₂O in the stratosphere affects ozone predominantly through NO_x-catalysed (NO_x = NO + NO₂) ozone-loss cycles. However, increases in N₂O do not necessarily lead to increases in NO_x, due to the interfering effects of other GHGs and ozone-depleting substances (ODSs). For example, the sink for NO_x is temperature dependent, so CO₂-induced cooling of the stratosphere decreases NO_x abundances. Nitrogen species incited large stratospheric ozone losses once the effects of CO₂-induced stratospheric cooling were removed. CH₄ weakens the ozone-depleting effectiveness of N₂O by producing reactive hydrogen species which (1) slow NO_x-catalysed ozone loss cycles in the upper stratosphere and (2) remove NO_x from the middle stratosphere through reactions to form HNO₃. Similarly, chlorine radicals produced by photolysis of ODSs such as the CFCs react with NO_x to form ClONO₂, thus reducing NO_x abundances. However, as the chlorine loading of the stratosphere decreases through the twenty-first century, the effect of chlorine on NO_x will become less important. Furthermore, N₂O is the dominant ODS currently emitted and is expected to remain so through the remainder of this century. The oxidation of CH₄ produces HO_x radicals (here: HO_x = H + OH + HO₂), which catalyse ozone destruction cycles, particularly in the upper stratosphere. The predominant effect of increasing CH₄ is to increase total column ozone by way of H₂O-induced stratospheric cooling in the middle stratosphere, which slows the temperature dependent gas-phase ozone loss cycles. In addition, increasing CH₄ increases the reaction rate which increases the rate of conversion of chlorine to the HCl reservoir and thereby slows the chlorine-catalysed ozone loss cycles throughout the stratosphere. Moreover, in the troposphere and very lower stratosphere, where the concentration of CO is sufficiently large, increased HO_x causes an increase in the reaction rates that lead to ozone production. Likewise, increased NO_x (from elevated N₂O concentrations) leads to ozone production in the troposphere and lower stratosphere (Revell et al. 2012).

A major fraction of ambient particulate matter arises from atmospheric gas-to-particle conversion. Attempts to reduce particulate matter levels require control of the same organic

and nitrogen oxide (NO_x) emissions that are precursors to urban and regional ozone formation. The common components of atmospheric particles, such as sulphate, nitrate, ammonium, organic compounds, crustal material, and water, reach the particulate phase by several different processes. Aside from the direct emission of particles into the atmosphere, gas-to-particle conversion processes play an essential role in determining the mass of airborne particulate matter. Such processes depend intimately on the organic and NO_x gas-phase chemistry that generate ozone (Meng, Dabdub, and Seinfeld 1997). The chemical coupling between ozone and particulate matter has implications for strategies to achieve the new ozone and particulate matter standards proposed by the US Environmental Protection Agency.

4.4. Diurnality and seasonality check

Both K1VHRR estimates and AMS measurements showed typical diurnal behaviour of instantaneous insolation in clear and cloudy days. This was purely sinusoidal for cloudless skies and disrupted sinusoidal in cloudy skies. Despite having one-to-one correspondences at most of the instances, both differ on certain occasions. Typical cases (Figure 4) were chosen for Bijapur, Nawagam and Ranchi in order to exemplify the possible reasons for the difference. In May 2008 at Bijapur, K1VHRR estimates showed a closer match with measurements at most instances except at 1330 local mean time (LMT) when there is a drop in measured insolation due to presence of clouds, while K1VHRR did not show the drop. The K1VHRR showed fewer overestimates in clear-skies during 1100 to 1330 LMT. Similar overestimates during 1100 to 1330 was also found for clear skies on 8 May 2008 at Nawagam and 5 December 2008 at Nawagam. A drop in K1VHRR insolation was found

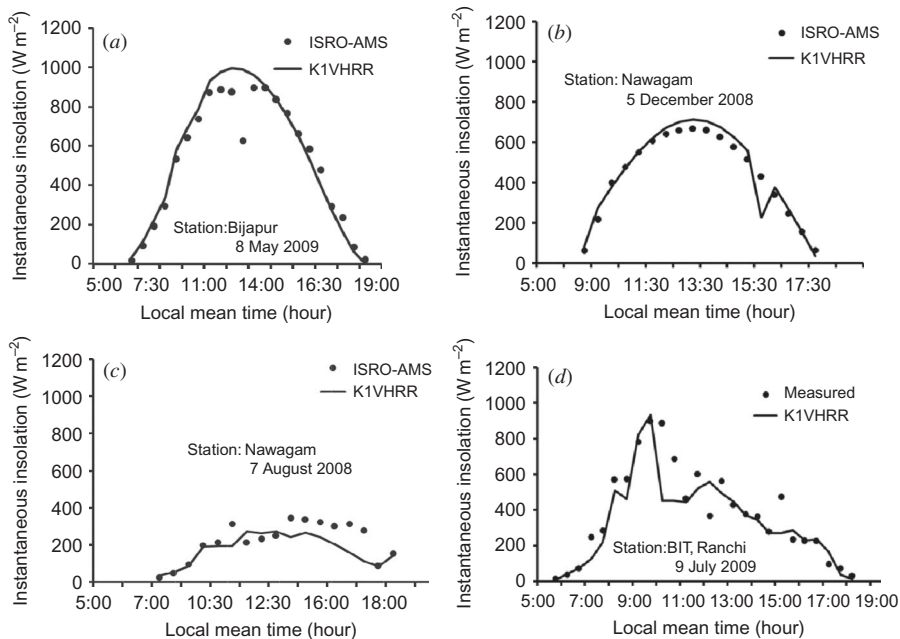


Figure 4. Comparison of diurnal estimates from K1VHRR with measurements from 0500 to 1900 local mean time (LMT) on typical clear-sky (6a and 6b) and cloudy days (6c and 6d).

on 5 December 2008, when AMS measurement showed clear-sky insolation. On a purely cloudy day on 7 August 2008, K1VHRR insolation was found to show that the effect of cloud exactly matched with measurements at most of the instances but largely differed during 1300 to 1630 LMT. In the cloudy skies on 9 July 2009, there were good correspondences between measurements and estimates in the morning hours up to 1130 LMT but they differed largely in magnitude in the afternoon hours.

In the present algorithm, a single AOD in a day per pixel was used. The diurnal variability of AOD at 550 nm was found to be low within $\pm 5\%$ of daily mean (Smirnov et al. 2002) at dust aerosol AERONET sites including Kanpur. Further, a larger diurnal variability of $\pm 20\%$ was reported over Pune (Pandithurai et al. 2007), Dehradun (Rana, Kant, and Dadhwal 2009), and the peninsular station (Srivastava et al. 2008) in India, as well as in China (Wang et al. 2004). The present cloud detection algorithm differentiates cloudy and clear pixels at all instances with 75–80% accuracy. The under- and over-representation within 20% inaccuracy of cloud detection may lead to an unexpected diurnal mismatch between estimates and measurements.

The daily insolation estimates extracted over western stations (Nawagam, Junagadh), the southern station (Bijapur), and the eastern station (Ranchi) were plotted for 365 calendar days (Figure 5) during the year 2009. All of the stations showed a wide variability in daily insolation from 0.2 to 28 MJ m^{-2} . The western stations showed a clear seasonal trend, but the fluctuation in daily insolation was the highest for the southern station followed by the eastern station, which is associated with more cloud dynamics.

The seasonal variability of monthly insolation was found to be lower and smoother than the variability of daily and 10 day averages. A set of regional statistics for the year 2009 such as minimum, maximum, range, mean, and standard deviation was computed on a given month over southeast Asia and is presented in Table 4. The minimum insolation varied from 1.11 (November) to 10.29 MJ m^{-2} (August). The maximum insolation was found to vary from 24.88 (October) to 29.09 MJ m^{-2} (June), but the highest and lowest

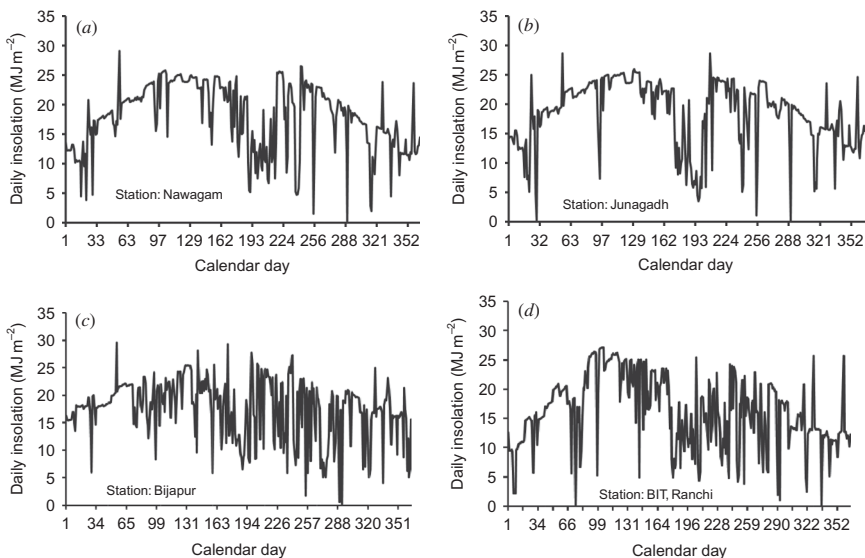


Figure 5. Variation of daily insolation at western (7a, 7b), southern (7c), and eastern (7d) stations over the Indian sub-continent during 2009.

ranges (= maximum – minimum) correspond to November (27.13 MJ m^{-2}) and August (16.63 MJ m^{-2}), respectively. Although the regional mean was lowest during January to December (13.35 MJ m^{-2}) and highest (19.12 – 19.15 MJ m^{-2}) during May to June, the standard deviations were higher during December to January (6.12 – 6.25 MJ m^{-2}) and lower (2.66 – 3.05 MJ m^{-2}) during May to June.

4.5. Assessment of monthly and annual insolation

The monthly insolation outputs are presented in Figure 6. A relatively low insolation regime (up to 7.5 MJ m^{-2}) was found over northern India during December and January in contrast to the higher regime over southern India (15 – 20 MJ m^{-2}). The effect of fog on insolation was evident over the Indo-Gangetic Plain (IGP) region during these two months. During February and March, the intra-tropical convergence zone (ITCZ) between 10° N and 10° S showed a very high insolation regime that was shifted to the west-central-eastern region of India in May. The higher insolation during February and March over the ITCZ drags trade winds from the southern to the northern hemisphere, bringing monsoon clouds during April and May. The high insolation regime further shifted over the Tibetan plateau in June and July when insolation decreased over the Indian sub-continent due to monsoon clouds. The higher insolation regime then shifted to the northwestern part of India in July and August, when a moderate-to-low insolation regime prevailed in the eastern and central regions. During October, a higher insolation regime was observed over the Arabian Sea and Indian Ocean. Later on, lower insolation prevailed over northern India with a low solar declination when the monsoon receded. The annual mean insolation varied from 5 to 25 MJ m^{-2} . A few high-insolation pockets hovering over southern, eastern, central, and west to northwestern regions were observed. A relatively lower-insolation regime was found over northern India

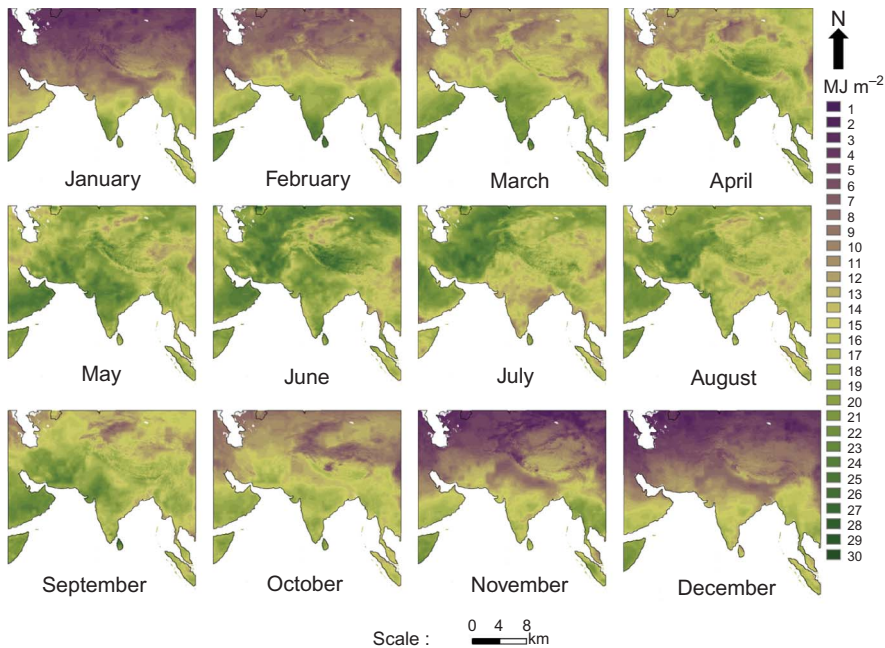


Figure 6. Monthly insolation distribution the over southeast Asia (44.5° E – 105.3° E , 9.8° S – 45.5° N) landmass from January to December 2009.

and the IGP region. A low-insolation regime was found over the Himalayan region but the Tibetan plateau showed a moderate-insolation regime.

The monthly insolation estimates from K1VHRR (along with ancillary inputs) during 2009 were compared with a global reanalysis field on monthly ‘surface incident shortwave radiation flux’ in MERRA (Modern Era Retrospective analysis for Research and Application) 2D data sets in a $2/3^\circ \times 1/2^\circ$ grid. MERRA is a NASA reanalysis for the satellite era using a major new version (V5) of the Goddard Earth Observing System (GEOS) Data Assimilation System (DAS). The goal of MERRA is to place satellite observations in a climate context with an emphasis on the hydrological cycle. MERRA instances provide meteorological and atmospheric data from an atmospheric observation reanalysis effort. The K1VHRR monthly insolation averages were resampled from 8 km to a MERRA 2D grid resolution. The spatial distribution of monthly differences showed that these were within 1.7 MJ m^{-2} for most of the Indian landmass but were large over China and adjacent territory. The annual difference (Figure 7) was also found to be of the same order for a major portion of the Indian landmass, except for a greater difference in northern and north-western India. While comparing annual insolation estimates from GMS (Geostationary Meteorological Satellite) observations over China with NCEP reanalysis data at a relatively coarser grid, Lu et al. (2010) also found relatively large differences (-4.32 MJ m^{-2}) beyond 30° N . The frequency distribution of annual insolation estimates over the Asia Mercator region is shown in Figure 8. The reanalysis data showed a narrow range from 15.1 to 25.9 MJ m^{-2} , but the range is wider from 8.2 to 22.4 MJ m^{-2} for K1VHRR estimates. Similar differences in probability density curves were also reported by Lu et al. (2010) between satellite estimates and reanalysis data. This suggests that reanalysis data have inherent limitations to produce the desired insolation distribution, which were better and consistently represented by geostationary satellite-based estimates.

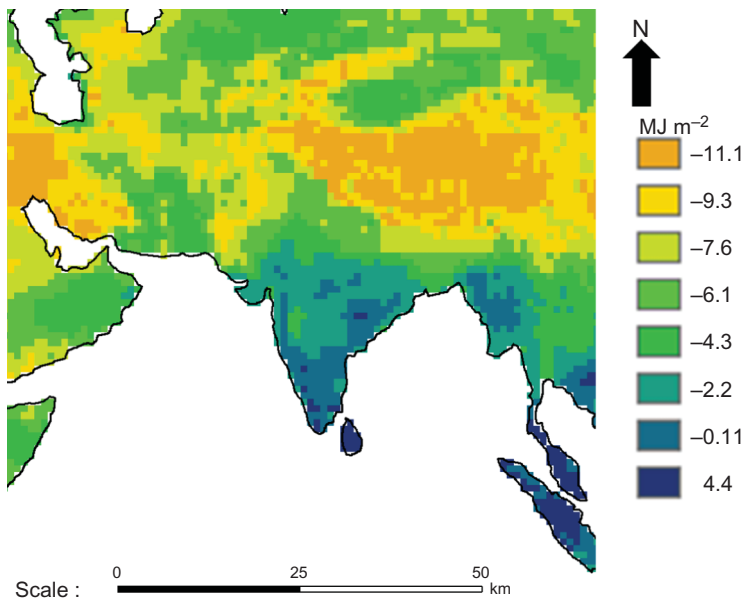


Figure 7. Difference in spatial distribution of annual average insolation of K1VHRR estimates and reanalysis data from MERRA 2D.

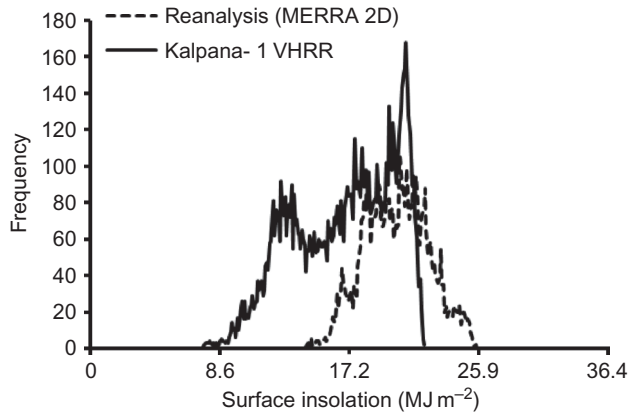


Figure 8. Comparison of frequency distribution of K1 VHRR estimates and reanalysis insolation.

5. Conclusions

The present algorithm estimated daily insolation with an overall error of 11.2% (2.05 MJ m^{-2}) of the measured mean, with $r = 0.93$ between estimates and measurements. The errors are expected to be reduced further for weekly, 10-day, and fortnightly to monthly averaging. Therefore, the present insolation product can be used in a more accurate way for studies that use weekly, fortnightly, or monthly insolation. This is a unique study where both power of remotely sensed observations from VHRR and the communication capability of DRT in the Kalpana-1 satellite were used for insolation estimation and collecting validation measurements from AMS towers, respectively. The present algorithm is easily extendable to future INSAT 3D observations to estimate insolation at 4 km. In future, INSAT 3D will have a six-channel 'Imager' with split-thermal infrared channels at 4 km, SWIR and MIR bands at 1 km. The additional bands and improvement in spatial resolution will provide better detection of the presence of clouds and cloud microphysical properties. The scheduled diurnal land aerosol product from INSAT 3D is expected to address the effect of aerosol diurnality. Moreover, the ozone and precipitable water products from the 'Sounder' would definitely curtail the requirements of global atmospheric products.

Acknowledgements

This work was carried out under the ISRO-GBP EMEVS project. We are grateful to A.S. Kirankumar, Director, Space Applications Centre (ISRO), for his constant support in this work. The first author is thankful to Dr S.S. Ray, Head, Agro-Ecosystems Division and Dr S. Panigrahy, Group Director for their critical suggestions while revising the manuscript. Thanks are due to Miss Tarjani Vyas of Gota Engineering College, Gujarat, for prototype scripting of KIRAN and Mr Sunayan Saha of IARI, New Delhi, for his help during validation. The help from Dr Manoj Kumar, BIT, Ranchi, for providing *in situ* data is gratefully acknowledged. The suggestions given by anonymous reviewers helped improve the quality of the article.

References

- Alexandris, D., C. Varotsos, K. Y. Kondratyev, and G. Chronopoulos. 1999. "On the Altitude Dependence of Solar Effective UV." *Physics and Chemistry of the Earth Part C-Solar-Terrestrial and Planetary Science* 24: 515–517.

- Anderson, J. G., M. W. David, J. B. Smith, and D. S. Sayres. 2012. "UV Dosage Levels in Summer: Increased Risk of Ozone Loss from Convectively Injected Water Vapor." *Science Express*, July 27 (10.1126/science.1222978): 1–5.
- Anonymous. 2005. "Task Team Report on Reception, Processing, Parameter Retrieval and Application of INSAT-3A/Kalpana Data: Campaign." Scientific report, Space Applications Centre (ISRO), Ahmedabad, India.
- Bhattacharya, B. K., C. B. S. Dutt, and J. S. Parihar. 2009. "INSAT Uplinked Agro-met Station — A Scientific Tool with a Network of Automated Micrometeorological Measurements for Soil–Canopy–Atmosphere Feedback Studies." In *ISPRS Archives XXXVIII-8/W3 Workshop Proceedings: Impact of Climate Change on Agriculture*, pp. 72–77. <http://www.isprs.org/proceedings/XXXVIII/8-W3/>
- Bhattacharya, B. K., S. Mallick, N. K. Patel, and J. S. Parihar. 2010. "Regional Evapotranspiration over Agricultural Land Using Remote Sensing Data from Indian Geostationary Meteorological Satellite." *Journal of Hydrology* 387: 65–80.
- Chen, J. M., J. Liu, J. Cihlar, and M. L. Goulden. 1999. "Daily Canopy Photosynthesis Model Through Temporal and Spatial Scaling for Remote Sensing Applications." *Ecological Modelling* 124: 99–119.
- Dagestad, K. F. 2004. "Mean Bias Deviation of the Heliosat Algorithm for Varying Cloud Properties and Sun-Ground-Satellite Geometry." *Theoretical and Applied Climatology* 79: 215–224.
- Dedieu, G., P. Y. Deschamps, and Y. H. Kerr. 1987. "Satellite Estimation of Solar Irradiance at the Surface of the Earth and of Surface Albedo Using a Physical Model Applied to METEOSAT Data." *Journal of Climate and Applied Meteorology* 26: 79–87.
- Deluisi, J. J., and J. Nimira. 1978. "Preliminary Comparison of Satellite UV and Surface-Based Umkehr Observations of the Vertical Distribution of Ozone in the Upper Stratosphere." *Journal of Geophysical Research* 83: 379–384.
- Gautier, C., G. Diak, and S. Masse. 1980. "A Simple Physical Model to Estimate Incident Solar Radiation at the Surface from GOES Satellite Data." *Journal of Applied Meteorology* 19: 1005–1012.
- Illera, P., A. Fernandez, and A. Perez. 1995. "A Simple Model for the Calculation of Global Solar Radiation Using Geostationary Satellite Data." *Atmospheric Research* 39: 79–90.
- Iqbal, M. 1983. *An Introduction to Solar Radiation*. Canada: Academic Press.
- Jacobs, J. M., D. A. Myers, M. C. Anderson, and G. R. Diak. 2000. "GOES Surface Insolation to Estimate Wetland Evapotranspiration." *Journal of Hydrology* 266: 53–65.
- Janjai, S., J. Lakasanaboonsong, M. Nunez, and A. Thongsathitya. 2005. "Development of a Method for Generating Operational Solar Radiation Maps from Satellite Data for a Tropical Environment." *Solar Energy* 78: 739–751.
- Kandirmaz, H. M., L. Yegingil, V. Pestemalci, and N. Emrahoglu. 2004. "Daily Global Solar Radiation Mapping of Turkey Using Meteosat Satellite Data." *International Journal of Remote Sensing* 25: 2159–2168.
- Katsambas, A., C. A. Varotsos, G. Veziryianni, and C. Antoniou. 1997. "Surface Solar Ultraviolet Radiation: A Theoretical Approach of the SUVR Reaching the Ground in Athens, Greece." *Environmental Science and Pollution Research* 4: 69–73.
- Kondratyev, K. Y. 1977. "Radiation Regime on Inclined Surfaces." Note Technique 152 (MF 79 N11613), World Meteorological Organization, Geneva, Switzerland.
- Kondratyev, K. Y., and C. A. Varotsos. 1996. "Global Total Ozone Dynamics – Impact on Surface Solar Ultraviolet Radiation Variability and Ecosystems." *Environmental Science and Pollution Research* 3: 205–209.
- Laurens, U. W., C. M. Van Sandwyk, J. M. De Jager, and J. Van Den Berg. 1995. "Accuracy of an Empirical Model for Estimating Daily Irradiance in South Africa from METEOSAT Imagery." *Agricultural and Forest Meteorology* 74: 75–86.
- Li, Z. 1998. "Influence of Absorbing Aerosols on the Inference of Solar Surface Radiation Budget and Cloud Absorption." *Journal of Climate* 11: 5–17.
- Lu, N., R. Liu, J. Liu, and S. Liang. 2010. "An Algorithm for Estimating Downward Shortwave Radiation from GMS Visible Imagery and Its Evaluation over China." *Journal of Geophysical Research* 115: 1–15.
- Meng, Z., D. Dabdub, and J. H. Seinfeld. 1997. "Chemical Coupling Between Atmospheric Ozone and Particulate Matter." *Science* 277: 116–119.

- Noia, M., C. F. Ratto, and R. Festa. 1993. "Solar Irradiance Estimation from Geostationary Data Using Statistical Methods." *Solar Energy* 51: 449–456.
- Otkin, J. A., M. C. Anderson, J. R. Mecikalski, and G. R. Diak. 2005. "Validation of GOES-Based Insolation Estimates Using Data from the United States Climate Reference Network." *Journal of Hydrometeorology* 6: 460–475.
- Pandithurai, G., R. T. Pinker, P. C. S. Devara, T. Takamura, and K. K. Dani. 2007. "Seasonal Asymmetry in Diurnal Variation of Aerosol Optical Characteristics over Pune, Western India." *Journal of Geophysical Research – Atmospheres* 112: 1–9. doi:10.1029/2006JD007803.
- Paulescu, M., and Z. Schlett. 2003. "A Simplified but Accurate Spectral Irradiance Model." *Theoretical and Applied Climatology* 75: 203–212.
- Perez, R., M. Kmeicik, C. Herig, and D. Renne. 2001. "Remote Monitoring of PV Performances Using Geostationary Satellites." *Solar Energy* 71: 255–261.
- Pinker, R. T., R. Frouin, and Z. Li. 1995. "A Review of Satellite Methods to Derive Surface Shortwave Irradiance." *Remote Sensing of Environment* 51: 105–124.
- Pinker, R. T., and I. Laszlo. 1992. "Modeling Surface Solar Irradiance for Satellite Applications on a Global Scale." *Journal of Applied Meteorology* 31: 105–124.
- Rana, S., Y. Kant, and V. K. Dadhwal. 2009. "Diurnal and Seasonal Variation of Aerosol Properties over Dehradun, India." *Aerosol and Air Quality* 9: 32–49.
- Revell, L. E., G. E. Bodeker, P. E. Huck, B. E. Williamson, and E. Rozanov. 2012. "The Sensitivity of Stratospheric Ozone Changes Through the 21st Century to N₂O and CH₄." *Atmospheric Chemistry and Physics Discuss* 12: 17583–17605.
- Rosema, A., L. Verhees, E. Putten, H. Gielen, T. Lack, J. Wood, A. Lane, J. Fannon, T. Estrela, M. Dimas, H. Bruin, A. Moene, and W. Meijninger. 2004. "European Energy and Water Balance Monitoring System." Scientific Report, EARS, Netherlands.
- Schadlich, S., F. M. Gottsche, and F. S. Olesen. 2001. "Influence of Land Surface Parameters and Atmosphere on METEOSAT Brightness Temperatures and Generation of Land Surface Temperature Maps by Temporally and Spatially Interpolating Atmospheric Correction." *Remote Sensing of Environment* 75: 39–46.
- Smirnov, A., B. N. Holben, T. F. Eck, I. Slutsker, B. Chatenet, and R. T. Pinker. 2002. "Diurnal Variability of Aerosol Optical Depth Observed at AERONET (Aerosol Robotic Network) Sites." *Geophysical Research Letters* 29: 2115–2118.
- Srivastava, A. K., P. C. S. Devara, Y. Jaya Rao, Y. Bhavanikumar, and D. N. Rao. 2008. "Aerosol Optical Depth, Ozone and Water Vapor Measurements over Gadanki, a Tropical Station in Peninsular India." *Aerosol and Air Quality Research* 8: 459–476.
- Tanahashi, S., H. Kawamura, T. Matsuura, T. Takahashi, and H. Yusa. 2001. "A System to Distribute Satellite Incident Solar Radiation in Real-Time." *Remote Sensing of Environment* 75: 412–422.
- Tarpley, J. D. 1979. "Estimating Incident Solar Radiation at the Surface from Geostationary Satellite Data." *Journal of Applied Meteorology* 18: 1172–1181.
- Turner, J., and J. Overland. 2009. "Contrasting Climate Change in Two Polar Regions." *Polar Research* 28: 146–164.
- Várnai, T., and A. Marshak. 2002. "Observations of Three-Dimensional Radiative Effects that Influence MODIS Cloud Optical Thickness Retrievals." *Journal of Atmospheric Sciences* 59: 1607–1618.
- Varotsos, C. 2005. "Airborne Measurements of Aerosol, Ozone and Solar Ultraviolet Irradiance in the Troposphere." *Journal of Geophysical Research – Atmospheres* 110. D9 Article Number: D09202. doi:10.1029/2004JD005397.
- Varotsos, C. A., G. J. Chronopoulos, S. Katsikis, and N. K. Sakellariou. 1995. "Further Evidence of the Role of Air-Pollution on Solar Ultraviolet Radiation Reaching the Ground." *International Journal of Remote Sensing* 16: 1883–1886.
- Varotsos, C. A., A. P. Cracknell, and C. Tzanis. 2012. "The Exceptional Ozone Depletion over the Arctic in January–March 2011." *Remote Sensing Letters* 3: 343–352.
- Varotsos, C., K. Y. Kondratyev, and S. Katsikis. 1995. "On the Relationship between Total Ozone and Solar Ultraviolet Radiation at St. Petersburg, Russia." *Geophysical Research Letters* 22: 3481–3484.
- Wang, J., X. Xia, P. Wang, and S. A. Christopher. 2004. "Diurnal Variability of Dust Aerosol Thickness and Angstrom Exponent over Dust Sources Region of China." *Geophysical Research Letters* 31: 8107–8110.